AIMS Mathematics, 8(11): 27210–27226.
DOI: 10.3934/math.20231392
Received: 25 July 2023
Revised: 07 September 2023
Accepted: 18 September 2023
Published: 25 September 2023

http://www.aimspress.com/journal/Math

Research article

On the identification of small anomaly in microwave imaging without homogeneous background information

Won-Kwang Park*

Department of Information Security, Cryptology, and Mathematics, Kookmin University, Seoul, 02707, Korea

* **Correspondence:** Email: parkwk@kookmin.ac.kr.

Abstract: For a successful application of subspace migration algorithm to retrieve the exact location and shape of small anomaly in microwave imaging, one must begin the reconstruction process under the assumption that complete information about the homogeneous background medium, such as background permittivity and conductivity, is available. In many studies, the statistical value of the background medium was adopted, raising the possibility of an incorrect value being applied. Thus, simulation results have been examined in order to identify cases in which an inaccurate location and shape of anomaly were retrieved. However, the theory explaining this phenomenon has not been investigated. In this paper, we apply an alternative wavenumber instead of the true one and identify the mathematical structure of the subspace migration imaging function for retrieving two-dimensional small anomaly by establishing a relationship with an infinite series of Bessel functions of the first kind. The revealed structure explains the reason behind the retrieval of an inaccurate location and shape of anomaly. The simulation results with synthetic data are presented to support the theoretical result.

Keywords: background information; microwave imaging; scattering parameter; subspace migration
Mathematics Subject Classification: 78A46

1. Introduction

Generally, one of the purposes of the microwave imaging is to localize or detect unknown objects from measured electromagnetic waves in the high-frequency regime (between 300 MHz and 300 GHz). Due to this reason, identification of the location and shape of unknown anomaly whose values of dielectric permittivity and electric conductivity differ from the homogeneous background medium from scattering parameter data is an important and interesting research topic in microwave imaging. Many authors have proposed various remarkable algorithms for retrieving information on anomaly for example, Born iterative method for reconstructing permittivity distribution [13] and

brain stroke detection [20], level-set method for shape reconstruction of unknown objects [16] and breast cancer detection [21], distorted iterated virtual experiments scheme for imaging unknown scatterers [28], conjugate gradient method for breast imaging [11], Levenberg-Marquardt technique for recovering parameter distribution [17]. We also refer to remarkable mathematical and experimental studies [1, 3, 12, 15, 26, 45–48]. However, the success of iteration-based algorithms significantly depends on the priori information and initial guess, which must be close to the unknown anomaly, refer to [25, 39].

For this reason, various non-iterative schemes in inverse scattering problems without a priori information about unknown anomaly have also been developed to retrieve the location and shape, such as a variational algorithm based on the inverse Fourier transform to retrieve small electromagnetic inhomogeneities [5, 6], direct sampling method for localizing small electromagnetic inhomogeneities [22,23] and anomaly detection in real-world experiment [43], factorization method for crack detection [10], shape reconstruction of unknown obstacles [18] and numerical study for anomaly imaging [33], linear sampling method for imaging of unknown scatters in limited-aperture problem [8] and crack-like defects [24], MUltiple SIgnal Classification (MUSIC) algorithm for identifying small anomalies [38], fast imaging of small targets in limited-aperture measurement configuration [35] and real-world application of anomaly detection [34], orthogonality sampling method for imaging unknown targets [40], qualitative microwave imaging [2], anomaly detection in microwave imaging [37] and topological derivative strategy for imaging crack-like defects [31] and retrieving unknown scatterers in 3D [27].

The subspace migration (SM) algorithm is a well-known, non-iterative imaging technique in both inverse scattering problem and microwave imaging. It has been applied successfully to the various problems such as localization of small targets [4], identification of extended objects [9], fast imaging of curve-like cracks [29, 30] and anomaly detection in microwave imaging [32, 36]. Throughout several studies, it has been confirmed that SM is a fast, robust and effective technique for retrieving unknown anomaly from scattering parameter data. However, for successful application in microwave imaging, accurate values of background permittivity and conductivity must be known because the exact background wavenumber value must be applied. Generally, most researchers have used the statistical values of the background material instead of the true ones and obtained inaccurate locations and shapes of anomaly. This can be examined through the results of numerical simulations but no reliable mathematical theory explaining this phenomenon has yet been developed.

In this paper, we apply the SM to retrieve unknown anomaly from scattering parameter data without complete information about the background material; that is, inaccurate values of background permittivity and conductivity are applied. To explain the appearance of an inaccurate location and shape of an anomaly, we show that the imaging function of the SM can be written as the infinite series of Bessel function of integer order, antenna arrangement and applied inaccurate values of background permittivity and conductivity. This enables us to theoretically explain the appearance of an inaccurate location and shape of an anomaly through the SM. To confirm the theoretical results, simulation results with inaccurate values of background permittivity and conductivity are also presented.

The rest of this paper is organized as follows. In Section 2, the two-dimensional direct problem and imaging function of the SM are introduced. The structure of the imaging function with inaccurate values of background permittivity and conductivity is revealed in Section 3. In Section 4, a set of numerical simulation results with synthetic data generated by CST STUDIO SUITE is presented.

Finally, a short conclusion is provided in Section 5.

2. Scattering parameter and imaging function of the subspace migration

Let D be a circle-like anomaly with radius α and center $\mathbf{r}_\star$ that is surrounded by a circular array of antennas $\mathbf{A}_n$ with location $\mathbf{a}_n$ and $|\mathbf{a}_n| = R$, $n = 1, 2, \cdots, N(> 2)$. Throughout this paper, we use Ω to denote a homogeneous domain filled by matching liquid such that $D \subset \Omega$ and assume that all materials D and Ω are nonmagnetic and classified by their value of dielectric permittivity and electric conductivity at a given angular frequency of operation ω, i.e., the value of magnetic permeability is constant for every $\mathbf{r} \in \Omega$ say, $\mu(\mathbf{r}) \equiv \mu_{\rm b} = 1.257 \times 10^{-6}$ H/m, refer to [41]. We use $\varepsilon_{\rm b}$ and $\sigma_{\rm b}$ to denote the background permittivity and conductivity, respectively. Analogously, let $\varepsilon_\star$ and $\sigma_\star$ be those of D. Then, we introduce the piecewise constant permittivity $\varepsilon(\mathbf{r})$ and conductivity $\sigma(\mathbf{r})$,

$$\varepsilon(\mathbf{r}) = \begin{cases} \varepsilon_\star & \text{for} \quad \mathbf{r} \in D, \\ \varepsilon_{\rm b} & \text{for} \quad \mathbf{r} \in \Omega \backslash D, \end{cases} \quad \text{and} \quad \sigma(\mathbf{r}) = \begin{cases} \sigma_\star & \text{for} \quad \mathbf{r} \in D, \\ \sigma_{\rm b} & \text{for} \quad \mathbf{r} \in \Omega \backslash D, \end{cases}$$

respectively. With this, let $k_{\rm b}$ be the background wavenumber that satisfies

$$k_{\rm b}^2 = \omega^2 \mu_{\rm b} \left(\varepsilon_{\rm b} - i \frac{\sigma_{\rm b}}{\omega} \right),$$

and further assume that

$$\omega \varepsilon_{\rm b} \gg \sigma_{\rm b} \quad \text{and} \quad \sqrt{\frac{\varepsilon_\star}{\varepsilon_{\rm b}}} < 1 + \frac{\text{wavelength}}{4\alpha}. \tag{2.1}$$

With this, the time-dependent, homogeneous, linear Maxwell Equations take the form:

$$\text{curl}\, \mathcal{E}(\mathbf{r}, t) = -\mu_{\rm b} \frac{\partial \mathcal{H}(\mathbf{r}, t)}{\partial t} \quad \text{and} \quad \text{curl}\, \mathcal{H}(\mathbf{r}, t) = \sigma_{\rm b} \mathcal{E}(\mathbf{r}, t) + \varepsilon_{\rm b} \frac{\partial \mathcal{E}(\mathbf{r}, t)}{\partial t}, \quad \mathbf{r} \in \Omega, \tag{2.2}$$

where $\mathcal{E}(\mathbf{r}, t) \in \mathbb{R}^3$ and $\mathcal{H}(\mathbf{r}, t) \in \mathbb{R}^3$ are the electric and magnetic fields, respectively. Here, we consider time-harmonic solutions to the (2.2) such that

$$\mathcal{E}(\mathbf{r}, t) = \text{Re}[\mathbf{E}(\mathbf{r}) e^{-i\omega t}] \quad \text{and} \quad \mathcal{H}(\mathbf{r}, t) = \text{Re}[\mathbf{H}(\mathbf{r}) e^{-i\omega t}], \quad \mathbf{r} \in \Omega, \ t > 0.$$

Then, $\mathbf{E}(\mathbf{r}) \in \mathbb{C}^3$ and $\mathbf{H}(\mathbf{r}) \in \mathbb{C}^3$ satisfy

$$\text{curl}\, \mathbf{E}(\mathbf{r}) = i\omega \mu_{\rm b} \mathbf{H}(\mathbf{r}) \quad \text{and} \quad \text{curl}\, \mathbf{H}(\mathbf{r}) = (\sigma_{\rm b} - i\omega \varepsilon_{\rm b}) \mathbf{E} \quad \text{in} \quad \Omega. \tag{2.3}$$

For a detailed description, we refer to [7].

Let $\mathbf{E}_{\rm inc}(k_{\rm b}, \mathbf{r}, \mathbf{a}_m)$ be the incident electric field due to the point current density $\mathbf{J}$ at $\mathbf{A}_m$. Then, based on (2.3), it satisfies

$$\begin{cases} \text{curl}\, \mathbf{E}_{\rm inc}(k_{\rm b}, \mathbf{r}, \mathbf{a}_m) = i\omega \mu_{\rm b} \mathbf{H}_{\rm inc}(k_{\rm b}, \mathbf{a}_m, \mathbf{r}), \\ \text{curl}\, \mathbf{H}_{\rm inc}(k_{\rm b}, \mathbf{r}, \mathbf{a}_m) = (\sigma_{\rm b} - i\omega \varepsilon_{\rm b}) \mathbf{E}_{\rm inc}(k_{\rm b}, \mathbf{r}, \mathbf{a}_m), \end{cases}$$

Analogously, let $\mathbf{E}_{\rm tot}(\mathbf{a}_n, \mathbf{r})$ be the total field measured at $\mathbf{A}_n$ in the presence of D that satisfies

$$\begin{cases} \text{curl}\, \mathbf{E}_{\rm tot}(k_{\rm b}, \mathbf{a}_n, \mathbf{r}) = i\omega \mu_{\rm b} \mathbf{H}_{\rm tot}(k_{\rm b}, \mathbf{a}_n, \mathbf{r}), \\ \text{curl}\, \mathbf{H}_{\rm tot}(k_{\rm b}, \mathbf{a}_n, \mathbf{r}) = (\sigma(\mathbf{r}) - i\omega \varepsilon(\mathbf{r})) \mathbf{E}_{\rm tot}(k_{\rm b}, \mathbf{a}_n, \mathbf{r}), \end{cases}$$

with transmission condition on ∂D.

Let $S(n,m)$ be the S-parameter (or scattering parameter), which is defined as the ratio of the output voltage (or reflected waves) at the $\mathbf{A}_n$ antenna and the input voltage (or incident waves) at the $\mathbf{A}_m$ (see [41] for instance). We use $S_{\text{inc}}(n,m)$ and $S_{\text{tot}}(n,m)$ to denote the incident and total field S-parameters, respectively, due to the absence and presence of D. Correspondingly, we let $S_{\text{scat}}(n,m) = S_{\text{tot}}(n,m) - S_{\text{inc}}(n,m)$ be the scattered field S-parameter. Then, based on [19], $S_{\text{scat}}(n,m)$ can be represented as follows:

$$S_{\text{scat}}(n,m) = -\frac{ik_0^2}{4\omega\mu_{\text{b}}}\int_{\Omega}\left(\frac{\varepsilon(\mathbf{r}')-\varepsilon_{\text{b}}}{\varepsilon_{\text{b}}}+i\frac{\sigma(\mathbf{r}')-\sigma_{\text{b}}}{\omega\varepsilon_{\text{b}}}\right)\mathbf{E}_{\text{inc}}(k_{\text{b}},\mathbf{r}',\mathbf{a}_m)\cdot\mathbf{E}_{\text{tot}}(k_{\text{b}},\mathbf{a}_n,\mathbf{r}')d\mathbf{r}',$$

where k_0 denotes the lossless background wave number that satisfies $k_0^2 = \omega^2\mu_{\text{b}}\varepsilon_{\text{b}}$.

In this paper, we adopt the simulation configuration introduced in [32, 43, 44]. Notice that the height of microwave machine can be said to be long enough, only the z-component of the incident and total fields can be handled based on the mathematical treatment of the scattering of time-harmonic electromagnetic waves from thin infinitely long cylindrical obstacles. Correspondingly, by denoting $\mathrm{E}_{\text{inc}}^{(z)}$ and $\mathrm{E}_{\text{tot}}^{(z)}$ as the z-components of the incident and total fields, respectively, $S_{\text{scat}}(n,m)$ can be written as follows:

$$S_{\text{scat}}(n,m) = -\frac{ik_0^2}{4\omega\mu_{\text{b}}}\int_{\Omega}\left(\frac{\varepsilon(\mathbf{r}')-\varepsilon_{\text{b}}}{\varepsilon_{\text{b}}}+i\frac{\sigma(\mathbf{r}')-\sigma_{\text{b}}}{\omega\varepsilon_{\text{b}}}\right)\mathrm{E}_{\text{inc}}^{(z)}(k_{\text{b}},\mathbf{r}',\mathbf{a}_m)\mathrm{E}_{\text{tot}}^{(z)}(k_{\text{b}},\mathbf{a}_n,\mathbf{r}')d\mathbf{r}'. \tag{2.4}$$

Unfortunately, exact expression of the field $\mathrm{E}_{\text{tot}}^{(z)}(k_{\text{b}},\mathbf{a}_n,\mathbf{r}')$ is unknown thus we cannot design the imaging function by using $S_{\text{scat}}(n,m)$ of (2.4) directly. Since the condition (2.1) holds, we can apply the Born approximation such that (see [42] for instance)

$$\mathrm{E}_{\text{tot}}^{(z)}(k_{\text{b}},\mathbf{a}_n,\mathbf{r}') = \mathrm{E}_{\text{inc}}^{(z)}(k_{\text{b}},\mathbf{a}_n,\mathbf{r}') + o(\alpha^2) = -\frac{i}{4}H_0^{(1)}(k_{\text{b}}|\mathbf{a}-\mathbf{r}'|) + o(\alpha^2),$$

where $H_0^{(1)}$ denotes the Hankel function of order zero of the first kind. Correspondingly, $S_{\text{scat}}(n,m)$ of (2.4) can be written as

$$\begin{aligned} S_{\text{scat}}(n,m) &= -\frac{ik_0^2}{4\omega\mu_{\text{b}}}\int_{D}\left(\frac{\varepsilon_\star-\varepsilon_{\text{b}}}{\varepsilon_{\text{b}}}+i\frac{\sigma_\star-\sigma_{\text{b}}}{\omega\varepsilon_{\text{b}}}\right)\mathrm{E}_{\text{inc}}^{(z)}(k_{\text{b}},\mathbf{r}',\mathbf{a}_m)\mathrm{E}_{\text{tot}}^{(z)}(k_{\text{b}},\mathbf{a}_n,\mathbf{r}')d\mathbf{r}' + o(\alpha^2k_0^2)\\ &= \frac{ik_0^2}{64\omega\mu_{\text{b}}}\int_{D}\left(\frac{\varepsilon_\star-\varepsilon_{\text{b}}}{\varepsilon_{\text{b}}}+i\frac{\sigma_\star-\sigma_{\text{b}}}{\omega\varepsilon_{\text{b}}}\right)H_0^{(1)}(k_{\text{b}}|\mathbf{a}_m-\mathbf{r}'|)H_0^{(1)}(k_{\text{b}}|\mathbf{a}_n-\mathbf{r}'|)d\mathbf{r}' + o(\alpha^2k_0^2). \end{aligned} \tag{2.5}$$

Now, we introduce the imaging function. To this end, let us generate the scattering matrix $\mathbb{K}$ such that

$$\mathbb{K} = \begin{bmatrix} 0 & S_{\text{scat}}(1,2) & \cdots & S_{\text{scat}}(1,N-1) & S_{\text{scat}}(1,N)\\ S_{\text{scat}}(2,1) & 0 & \cdots & S_{\text{scat}}(2,N-1) & S_{\text{scat}}(2,N)\\ \vdots & \vdots & \ddots & \vdots & \vdots\\ S_{\text{scat}}(N,1) & S_{\text{scat}}(N,2) & \cdots & S_{\text{scat}}(N,N-1) & 0 \end{bmatrix}. \tag{2.6}$$

See [32] for an explanation of why the diagonal elements of $\mathbb{K}$ are set to zero. Since there is a single, small anomaly, the singular value decomposition (SVD) of $\mathbb{K}$ can be written as

$$\mathbb{K} = \mathbb{U}\mathbb{D}\mathbb{V}^* = \sum_{n=1}^{N}\tau_n\mathbf{U}_n\mathbf{V}_n^* \approx \tau_1\mathbf{U}_1\mathbf{V}_1^*, \tag{2.7}$$

where $*$ denotes the mark of Hermitian, τ_n are the singular values and $\mathbf{U}_n$ and $\mathbf{V}_n$ are the left and right singular vectors of $\mathbb{K}$, respectively. Then, on the basis of (2.5) and (2.7), we define a unit vector: For each $\mathbf{r} \in \Omega$,

$$\mathbf{W}(k_\mathrm{b}, \mathbf{r}) = \frac{\mathbf{F}(k_\mathrm{b}, \mathbf{r})}{|\mathbf{F}(k_\mathrm{b}, \mathbf{r})|}, \quad \mathbf{F}(k_\mathrm{b}, \mathbf{r}) = \left[H_0^{(1)}(k_\mathrm{b}|\mathbf{a}_1 - \mathbf{r}|), H_0^{(1)}(k_\mathrm{b}|\mathbf{a}_2 - \mathbf{r}|), \ldots, H_0^{(1)}(k_\mathrm{b}|\mathbf{a}_N - \mathbf{r}|)\right]^T. \tag{2.8}$$

With this, we introduce the following imaging function of the SM: For each $\mathbf{r} \in \Omega$,

$$\mathfrak{F}(k_\mathrm{b}, \mathbf{r}) = \left|\langle \mathbf{W}(k_\mathrm{b}, \mathbf{r}), \mathbf{U}_1\rangle\langle \mathbf{W}(k_\mathrm{b}, \mathbf{r}), \overline{\mathbf{V}}_1\rangle\right|, \tag{2.9}$$

where $\langle \mathbf{U}, \mathbf{V}\rangle = \mathbf{U}^*\mathbf{V}$ and $\overline{\mathbf{V}}_1$ denotes the complex conjugate of $\mathbf{V}_1$. Then, based on [4]

$$\langle \mathbf{W}(k_\mathrm{b}, \mathbf{r}), \mathbf{U}_1\rangle \approx 1 \quad \text{and} \quad \langle \mathbf{W}(k_\mathrm{b}, \mathbf{r}), \overline{\mathbf{V}}_1\rangle \approx 1 \quad \text{when} \quad \mathbf{r} \in D,$$

and the orthonormal property of singular vectors, the value of $\mathfrak{F}(k_\mathrm{b}, \mathbf{r})$ will be close to 1 when $\mathbf{r} \in D$ and less than 1 at $\mathbf{r} \in \Omega\backslash D$, so the location and outline shape of D can be identified through the map of $\mathfrak{F}(k_\mathrm{b}, \mathbf{r})$.

Let us emphasize that, to generate the test vector $\mathbf{W}(k_\mathrm{b}, \mathbf{r})$ of (2.8), the exact value of k_b must be known, i.e., a priori information of the ε_b and σ_b must be available. However, because these values are statistical, the exact value may not be unknown. For this reason, we assume that the exact values of ε_b and σ_b are unknown and apply an alternative value k_a instead of the true k_b and set a unit test vector $\mathbf{W}(k_\mathrm{a}, \mathbf{r})$ from (2.8). Then, by using the imaging function $\mathfrak{F}(k_\mathrm{a}, \mathbf{r})$ from (2.9), the exact location and shape of D cannot be retrieved. Fortunately, we can recognize the existence of D and the identified location is shifted in a specific direction.

3. Analysis of the imaging function

In this section, we explore the structure of the imaging function $\mathfrak{F}(k_\mathrm{a}, \mathbf{r})$ to explain that retrieved location of D is shifted in a specific direction and size is smaller or larger than the true anomaly. To explain this phenomenon, we explore the structure of the imaging function.

Theorem 3.1. *Let $\boldsymbol{\theta}_n = \mathbf{a}_n/|\mathbf{a}_n| = (\cos\theta_n, \sin\theta_n)$ and $k_\mathrm{b}\mathbf{r}' - k_\mathrm{a}\mathbf{r} = |k_\mathrm{b}\mathbf{r}' - k_\mathrm{a}\mathbf{r}|(\cos\phi, \sin\phi)$. If $\mathbf{a}_n$ satisfies $|\mathbf{a}_n - \mathbf{r}| \gg \{1/4|k_\mathrm{a}|, 1/4|k_\mathrm{b}|\}$ for all $n = 1, 2, \cdots, N$, then $\mathfrak{F}(\mathbf{r}, k_\mathrm{a})$ can be represented as follows:*

$$\mathfrak{F}(k_\mathrm{a}, \mathbf{r}) = \frac{N}{(N-1)\,\mathrm{area}(D)}\left|\int_D \left(J_0(|k_\mathrm{b}\mathbf{r}' - k_\mathrm{a}\mathbf{r}|) + \frac{\Psi(k_\mathrm{b}, k_\mathrm{a}, \mathbf{r})}{N}\right)^2 d\mathbf{r}' \right.$$
$$\left. - \frac{1}{N}\int_D \left(J_0(2|k_\mathrm{b}\mathbf{r}' - k_\mathrm{a}\mathbf{r}|) + \frac{\Psi(2k_\mathrm{b}, 2k_\mathrm{a}, \mathbf{r})}{N}\right) d\mathbf{r}'\right| + o(\alpha^2 k_0^2), \tag{3.1}$$

where J_s denotes the Bessel function of order s and

$$\Psi(k_\mathrm{b}, k_\mathrm{a}, \mathbf{r}) = \sum_{n=1}^{N}\sum_{s=-\infty, s\neq 0}^{\infty} i^s J_s(|k_\mathrm{b}\mathbf{r}' - k_\mathrm{a}\mathbf{r}|)e^{is(\theta_n - \phi)}.$$

Proof. Since $\mathbb{K} \approx \tau_1 \mathbf{U}_1 \mathbf{V}_1^*$, we can examine that

$$\mathfrak{F}(k_\mathrm{b}, \mathbf{r}) = \left|\langle \mathbf{W}(k_\mathrm{a}, \mathbf{r}), \mathbf{U}_1 \rangle \langle \mathbf{W}(k_\mathrm{a}, \mathbf{r}), \overline{\mathbf{V}}_1 \rangle\right| = \left|\mathbf{W}(k_\mathrm{a}, \mathbf{r})^* \mathbf{U}_1 \mathbf{V}_1^* \overline{\mathbf{W}(k_\mathrm{a}, \mathbf{r})}\right| \approx \left|\frac{1}{\tau_1} \mathbf{W}(k_\mathrm{a}, \mathbf{r})^* \mathbb{K} \overline{\mathbf{W}(k_\mathrm{a}, \mathbf{r})}\right|.$$

Based on the assumption $|\mathbf{a}_n - \mathbf{r}| \gg \{1/4|k_\mathrm{a}|, 1/4|k_\mathrm{b}|\}$ for all $n = 1, 2, \cdots, N$, the following asymptotic forms of the Hankel function hold (see [14, Theorem 2.5], for instance)

$$H_0^{(1)}(k_\mathrm{b}|\mathbf{r} - \mathbf{r}'|) = \frac{(1-i)e^{-ik_\mathrm{b}|\mathbf{r}|}}{\sqrt{k_\mathrm{b}\pi|\mathbf{a}_n|}} e^{ik_\mathrm{b}\boldsymbol{\theta}_n \cdot \mathbf{r}'} + O(1) \quad \text{and} \quad H_0^{(1)}(k_\mathrm{a}|\mathbf{r} - \mathbf{r}'|) = \frac{(1-i)e^{-ik_\mathrm{a}|\mathbf{r}|}}{\sqrt{k_\mathrm{a}\pi|\mathbf{a}_n|}} e^{ik_\mathrm{a}\boldsymbol{\theta}_n \cdot \mathbf{r}'} + O(1). \quad (3.2)$$

Then, $\mathbf{W}(k_\mathrm{a}, \mathbf{r})$ and $\mathbb{K}$ can be represented as

$$\mathbf{W}(k_\mathrm{a}, \mathbf{r}) = \frac{1}{\sqrt{N}} \begin{bmatrix} e^{ik_\mathrm{a}\boldsymbol{\theta}_1 \cdot \mathbf{r}} + O(1) \\ e^{ik_\mathrm{a}\boldsymbol{\theta}_2 \cdot \mathbf{r}} + O(1) \\ \vdots \\ e^{ik_\mathrm{a}\boldsymbol{\theta}_N \cdot \mathbf{r}} + O(1) \end{bmatrix}$$

and

$$\mathbb{K} = C \begin{bmatrix} 0 & \int_D e^{ik_\mathrm{b}(\boldsymbol{\theta}_1 + \boldsymbol{\theta}_2)\cdot \mathbf{r}'} d\mathbf{r}' + o(\alpha^2 k_0^2) & \cdots & \int_D e^{ik_\mathrm{b}(\boldsymbol{\theta}_1 + \boldsymbol{\theta}_N)\cdot \mathbf{r}'} d\mathbf{r}' + o(\alpha^2 k_0^2) \\ \int_D e^{ik_\mathrm{b}(\boldsymbol{\theta}_2 + \boldsymbol{\theta}_1)\cdot \mathbf{r}'} d\mathbf{r}' + o(\alpha^2 k_0^2) & 0 & \cdots & \int_D e^{ik_\mathrm{b}(\boldsymbol{\theta}_2 + \boldsymbol{\theta}_N)\cdot \mathbf{r}'} d\mathbf{r}' + o(\alpha^2 k_0^2) \\ \vdots & \vdots & \ddots & \vdots \\ \int_D e^{ik_\mathrm{b}(\boldsymbol{\theta}_N + \boldsymbol{\theta}_1)\cdot \mathbf{r}'} d\mathbf{r}' + o(\alpha^2 k_0^2) & \int_D e^{ik_\mathrm{b}(\boldsymbol{\theta}_N + \boldsymbol{\theta}_2)\cdot \mathbf{r}'} d\mathbf{r}' + o(\alpha^2 k_0^2) & \cdots & 0 \end{bmatrix},$$

respectively. Here the constant C is given by

$$C = \frac{k_0^2 e^{-2ik_\mathrm{b}R}}{32 k_\mathrm{b} \omega \mu_\mathrm{b} \pi R} \left(\frac{\varepsilon_\star - \varepsilon_\mathrm{b}}{\varepsilon_\mathrm{b}} + i \frac{\sigma_\star - \sigma_\mathrm{b}}{\omega \varepsilon_\mathrm{b}} \right).$$

Note that, since the following JacobiAnger expansion formula holds uniformly

$$e^{ix\cos\theta} = \sum_{s=-\infty}^{\infty} i^s J_s(x) e^{is\theta} = J_0(x) + \sum_{s=-\infty, s\neq 0}^{\infty} i^s J_s(x) e^{is\theta}, \quad (3.3)$$

we have for $n = 1, 2, \cdots, N$

$$\begin{aligned} \sum_{n=1}^{N} e^{i\boldsymbol{\theta}_n \cdot (k_\mathrm{b}\mathbf{r}' - k_\mathrm{a}\mathbf{r})} &= \sum_{n=1}^{N} e^{i|k_\mathrm{b}\mathbf{r}' - k_\mathrm{a}\mathbf{r}|\cos(\theta_n - \phi)} = \sum_{n=1}^{N} \left(J_0(|k_\mathrm{b}\mathbf{r}' - k_\mathrm{a}\mathbf{r}|) + \sum_{s=-\infty, s\neq 0}^{\infty} i^s J_s(|k_\mathrm{b}\mathbf{r}' - k_\mathrm{a}\mathbf{r}|) e^{is(\theta_n - \phi)} \right) \\ &= N J_0(|k_\mathrm{b}\mathbf{r}' - k_\mathrm{a}\mathbf{r}|) + \Psi(k_\mathrm{b}, k_\mathrm{a}, \mathbf{r}) \end{aligned}$$

and correspondingly,

$$\mathbf{W}(k_{\mathrm{a}},\mathbf{r})^{*}\mathbb{K}=\frac{C}{\sqrt{N}}\begin{bmatrix}\displaystyle\int_D e^{ik_{\mathrm{b}}\boldsymbol{\theta}_1\cdot\mathbf{r}'}\sum_{n=1}^{N}\left(e^{i\boldsymbol{\theta}_n(k_{\mathrm{b}}\mathbf{r}'-k_{\mathrm{a}}\mathbf{r})}-e^{i\boldsymbol{\theta}_1(k_{\mathrm{b}}\mathbf{r}'-k_{\mathrm{a}}\mathbf{r})}\right)d\mathbf{r}'+o(\alpha^2k_0^2)\\ \displaystyle\int_D e^{ik_{\mathrm{b}}\boldsymbol{\theta}_2\cdot\mathbf{r}'}\sum_{n=1}^{N}\left(e^{i\boldsymbol{\theta}_n(k_{\mathrm{b}}\mathbf{r}'-k_{\mathrm{a}}\mathbf{r})}-e^{i\boldsymbol{\theta}_2(k_{\mathrm{b}}\mathbf{r}'-k_{\mathrm{a}}\mathbf{r})}\right)d\mathbf{r}'+o(\alpha^2k_0^2)\\ \vdots\\ \displaystyle\int_D e^{ik_{\mathrm{b}}\boldsymbol{\theta}_1\cdot\mathbf{r}'}\sum_{n=1}^{N}\left(e^{i\boldsymbol{\theta}_n(k_{\mathrm{b}}\mathbf{r}'-k_{\mathrm{a}}\mathbf{r})}-e^{i\boldsymbol{\theta}_N(k_{\mathrm{b}}\mathbf{r}'-k_{\mathrm{a}}\mathbf{r})}\right)d\mathbf{r}'+o(\alpha^2k_0^2)\end{bmatrix}^{T}$$

$$=\frac{C}{\sqrt{N}}\begin{bmatrix}\displaystyle\int_D e^{ik_{\mathrm{b}}\boldsymbol{\theta}_1\cdot\mathbf{r}'}\left(NJ_0(|k_{\mathrm{b}}\mathbf{r}'-k_{\mathrm{a}}\mathbf{r}|)+\Psi(k_{\mathrm{b}},k_{\mathrm{a}},\mathbf{r})-e^{i\boldsymbol{\theta}_1(k_{\mathrm{b}}\mathbf{r}'-k_{\mathrm{a}}\mathbf{r})}\right)d\mathbf{r}'+o(\alpha^2k_0^2)\\ \displaystyle\int_D e^{ik_{\mathrm{b}}\boldsymbol{\theta}_2\cdot\mathbf{r}'}\left(NJ_0(|k_{\mathrm{b}}\mathbf{r}'-k_{\mathrm{a}}\mathbf{r}|)+\Psi(k_{\mathrm{b}},k_{\mathrm{a}},\mathbf{r})-e^{i\boldsymbol{\theta}_2(k_{\mathrm{b}}\mathbf{r}'-k_{\mathrm{a}}\mathbf{r})}\right)d\mathbf{r}'+o(\alpha^2k_0^2)\\ \vdots\\ \displaystyle\int_D e^{ik_{\mathrm{b}}\boldsymbol{\theta}_1\cdot\mathbf{r}'}\left(NJ_0(|k_{\mathrm{b}}\mathbf{r}'-k_{\mathrm{a}}\mathbf{r}|)+\Psi(k_{\mathrm{b}},k_{\mathrm{a}},\mathbf{r})-e^{i\boldsymbol{\theta}_N(k_{\mathrm{b}}\mathbf{r}'-k_{\mathrm{a}}\mathbf{r})}\right)d\mathbf{r}'+o(\alpha^2k_0^2)\end{bmatrix}^{T}.$$

With this, we can evaluate

$$\mathbf{W}(k_{\mathrm{a}},\mathbf{r})^{*}\mathbb{K}\overline{\mathbf{W}(k_{\mathrm{a}},\mathbf{r})}$$

$$=\frac{C}{N}\begin{bmatrix}\displaystyle\int_D e^{ik_{\mathrm{b}}\boldsymbol{\theta}_1\cdot\mathbf{r}'}\left(NJ_0(|k_{\mathrm{b}}\mathbf{r}'-k_{\mathrm{a}}\mathbf{r}|)+\Psi(k_{\mathrm{b}},k_{\mathrm{a}},\mathbf{r})-e^{i\boldsymbol{\theta}_1(k_{\mathrm{b}}\mathbf{r}'-k_{\mathrm{a}}\mathbf{r})}\right)d\mathbf{r}'+o(\alpha^2k_0^2)\\ \displaystyle\int_D e^{ik_{\mathrm{b}}\boldsymbol{\theta}_2\cdot\mathbf{r}'}\left(NJ_0(|k_{\mathrm{b}}\mathbf{r}'-k_{\mathrm{a}}\mathbf{r}|)+\Psi(k_{\mathrm{b}},k_{\mathrm{a}},\mathbf{r})-e^{i\boldsymbol{\theta}_2(k_{\mathrm{b}}\mathbf{r}'-k_{\mathrm{a}}\mathbf{r})}\right)d\mathbf{r}'+o(\alpha^2k_0^2)\\ \vdots\\ \displaystyle\int_D e^{ik_{\mathrm{b}}\boldsymbol{\theta}_N\cdot\mathbf{r}'}\left(NJ_0(|k_{\mathrm{b}}\mathbf{r}'-k_{\mathrm{a}}\mathbf{r}|)+\Psi(k_{\mathrm{b}},k_{\mathrm{a}},\mathbf{r})-e^{i\boldsymbol{\theta}_N(k_{\mathrm{b}}\mathbf{r}'-k_{\mathrm{a}}\mathbf{r})}\right)d\mathbf{r}'+o(\alpha^2k_0^2)\end{bmatrix}^{T}\begin{bmatrix}e^{-ik_{\mathrm{a}}\boldsymbol{\theta}_1\cdot\mathbf{r}}+O(1)\\ e^{-ik_{\mathrm{a}}\boldsymbol{\theta}_2\cdot\mathbf{r}}+O(1)\\ \vdots\\ e^{-ik_{\mathrm{a}}\boldsymbol{\theta}_N\cdot\mathbf{r}}+O(1)\end{bmatrix}$$

$$=\frac{C}{N}\int_D\sum_{n=1}^{N}e^{i\boldsymbol{\theta}_n\cdot(k_{\mathrm{b}}\mathbf{r}'-k_{\mathrm{a}}\mathbf{r})}\left(NJ_0(|k_{\mathrm{b}}\mathbf{r}'-k_{\mathrm{a}}\mathbf{r}|)+\Psi(k_{\mathrm{b}},k_{\mathrm{a}},\mathbf{r})-e^{i\boldsymbol{\theta}_n(k_{\mathrm{b}}\mathbf{r}'-k_{\mathrm{a}}\mathbf{r})}\right)d\mathbf{r}'+o(\alpha^2k_0^2)$$

$$=\frac{C}{N}\int_D e^{i\boldsymbol{\theta}_n\cdot(k_{\mathrm{b}}\mathbf{r}'-k_{\mathrm{a}}\mathbf{r})}\Big(NJ_0(|k_{\mathrm{b}}\mathbf{r}'-k_{\mathrm{a}}\mathbf{r}|)+\Psi(k_{\mathrm{b}},k_{\mathrm{a}},\mathbf{r})\Big)d\mathbf{r}'-\frac{C}{N}\int_D\sum_{n=1}^{N}e^{2i\boldsymbol{\theta}_n\cdot(k_{\mathrm{b}}\mathbf{r}'-k_{\mathrm{a}}\mathbf{r})}d\mathbf{r}'+o(\alpha^2k_0^2)$$

$$=\frac{C}{N}\int_D\left[\Big(NJ_0(|k_{\mathrm{b}}\mathbf{r}'-k_{\mathrm{a}}\mathbf{r}|)+\Psi(k_{\mathrm{b}},k_{\mathrm{a}},\mathbf{r})\Big)^2d\mathbf{r}'-\Big(NJ_0(2|k_{\mathrm{b}}\mathbf{r}'-k_{\mathrm{a}}\mathbf{r}|)+\Psi(2k_{\mathrm{b}},2k_{\mathrm{a}},\mathbf{r})\Big)\right]d\mathbf{r}'+o(\alpha^2k_0^2).$$

Hence,

$$\langle\mathbf{W}(k_{\mathrm{a}},\mathbf{r}),\mathbf{U}_1\rangle\langle\mathbf{W}(k_{\mathrm{a}},\mathbf{r}),\overline{\mathbf{V}}_1\rangle=\frac{CN}{\tau_1}\int_D\left(J_0(|k_{\mathrm{b}}\mathbf{r}'-k_{\mathrm{a}}\mathbf{r}|)+\frac{\Psi(k_{\mathrm{b}},k_{\mathrm{a}},\mathbf{r})}{N}\right)^2d\mathbf{r}'$$
$$-\frac{C}{\tau_1}\int_D\left(J_0(2|k_{\mathrm{b}}\mathbf{r}'-k_{\mathrm{a}}\mathbf{r}|)+\frac{\Psi(2k_{\mathrm{b}},2k_{\mathrm{a}},\mathbf{r})}{N}\right)d\mathbf{r}'+o(\alpha^2k_0^2).$$

Since $\langle \mathbf{W}(\mathbf{r}), \mathbf{U}_1 \rangle \langle \mathbf{W}(\mathbf{r}), \overline{\mathbf{V}}_1 \rangle = 1$, $J_0(|k_\mathrm{b}\mathbf{r}' - k_\mathrm{a}\mathbf{r}|) = J_0(2|k_\mathrm{b}\mathbf{r}' - k_\mathrm{a}\mathbf{r}|) = 1$ and $\Psi(k_\mathrm{b}, k_\mathrm{a}, \mathbf{r}) = \Psi(2k_\mathrm{b}, 2k_\mathrm{a}, \mathbf{r}) = 0$ when $k_\mathrm{b}\mathbf{r}' = k_\mathrm{a}\mathbf{r}$, we have

$$\frac{CN}{\tau_1} \int_D d\mathbf{r}' - \frac{C}{\tau_1} \int_D d\mathbf{r}' + o(\alpha^2 k_0^2) = 1 \quad \text{implies} \quad C = \frac{\tau_1}{(N-1)\,\mathrm{area}(D)} + o(\alpha^2 k_0^2).$$

Therefore,

$$\begin{aligned}\langle \mathbf{W}(\mathbf{r}), \mathbf{U}_1 \rangle \langle \mathbf{W}(\mathbf{r}), \overline{\mathbf{V}}_1 \rangle = {} & \frac{N}{(N-1)\,\mathrm{area}(D)} \int_D \left(J_0(|k_\mathrm{b}\mathbf{r}' - k_\mathrm{a}\mathbf{r}|) + \frac{\Psi(k_\mathrm{b}, k_\mathrm{a}, \mathbf{r})}{N} \right)^2 d\mathbf{r}' \\ & - \frac{1}{(N-1)\,\mathrm{area}(D)} \int_D \left(J_0(2|k_\mathrm{b}\mathbf{r}' - k_\mathrm{a}\mathbf{r}|) + \frac{\Psi(2k_\mathrm{b}, 2k_\mathrm{a}, \mathbf{r})}{N} \right) d\mathbf{r}' + o(\alpha^2 k_0^2).\end{aligned}$$

With this, we can obtain the structure (3.1). □

From the derived structure (3.1), we can observe that since $J_0(|k_\mathrm{b}\mathbf{r}' - k_\mathrm{a}\mathbf{r}|) = 1$ and $\Psi(k_\mathrm{b}, k_\mathrm{a}, \mathbf{r}) = 0$ when $\mathbf{r} = (k_\mathrm{b}/k_\mathrm{a})\mathbf{r}'$ for $\mathbf{r}' \in D$, an inaccurate location and shape of D must be retrieved through the map of $\mathfrak{F}(k_\mathrm{a}, \mathbf{r})$. This is the theoretical reason why an inaccurate location and shape of the anomaly is retrieved when inaccurate values of ε_b and σ_b were applied. Further properties will be discussed in the simulation results.

4. Simulation results

Here, we present simulation results to support the result in Theorem 3.1. To this end, a circular array of $N = 16$ antennas $\mathbf{A}_n$ is used to transmit and receive signals operated at $f = 1.24\,\mathrm{GHz}$. The location of the antennas was set to

$$\mathbf{a}_n = 0.09\,\mathrm{m}(\cos\theta_n, \sin\theta_n), \quad \theta_n = \frac{2\pi(n-1)}{N}$$

and the search domain Ω was selected as a square region $(-0.1\,\mathrm{m}, 0.1\,\mathrm{m}) \times (-0.1\,\mathrm{m}, 0.1\,\mathrm{m})$ with $(\varepsilon_\mathrm{b}, \sigma_\mathrm{b}) = (20\varepsilon_0, 0.2\,\mathrm{S/m})$. Here, $\varepsilon_0 = 8.854 \times 10^{-12}\,\mathrm{F/m}$ is the vacuum permittivity. Correspondingly, the exact value of the background wavenumber is $k_\mathrm{b} = 116.5273 + 8.4020i$. For anomalies, we selected two small balls D_1 and D_2 with centers $\mathbf{r}_1 = (0.01\,\mathrm{m}, 0.03\,\mathrm{m})$ and $\mathbf{r}_2 = (-0.04\,\mathrm{m}, -0.02\,\mathrm{m})$, same radii $\alpha = 0.01\,\mathrm{m}$ and material properties $(\varepsilon_1, \sigma_1) = (55\varepsilon_0, 1.2\,\mathrm{S/m})$ and $(\varepsilon_2, \sigma_2) = (45\varepsilon_0, 1.0\,\mathrm{S/m})$. With these settings, the measurement data $S_\mathrm{scat}(n, m)$ of (2.6) and the incident field data of (2.8) were generated by CST STUDIO SUITE.

Example 4.1. *(Only exact value of ε_b is unknown) First, we consider the case where only the exact value of ε_b is unknown. Instead, of the application of ε_b, we applied alternative values ε_a and corresponding wavenumber*

$$k_\mathrm{a} = \omega \sqrt{\mu_\mathrm{b} \left(\varepsilon_\mathrm{a} - i\frac{\sigma_\mathrm{b}}{\omega} \right)}.$$

Note that we already assumed that $\omega\varepsilon_\mathrm{b} \gg \sigma_\mathrm{b}$. Thus, if the condition $\omega\varepsilon_\mathrm{a} \gg \sigma_\mathrm{b}$ is satisfied, the identified location becomes

$$\mathbf{r} = \left(\frac{k_\mathrm{b}}{k_\mathrm{a}} \right) \mathbf{r}' = \sqrt{\frac{\omega\varepsilon_\mathrm{b} - i\sigma_\mathrm{b}}{\omega\varepsilon_\mathrm{a} - i\sigma_\mathrm{b}}}\,\mathbf{r}' \approx \sqrt{\frac{\varepsilon_\mathrm{b}}{\varepsilon_\mathrm{a}}}\,\mathbf{r}' \quad \textit{for each} \quad \mathbf{r}' \in D_1. \tag{4.1}$$

Hence, identified anomalies will be concentrated at the origin and their retrieved sizes will be smaller than the true one when $\varepsilon_a > \varepsilon_b$. Otherwise, identified anomalies will be far from the origin and their retrieved sizes will be larger than the true one when $\varepsilon_a < \varepsilon_b$. See Figure 1 for a related illustration.

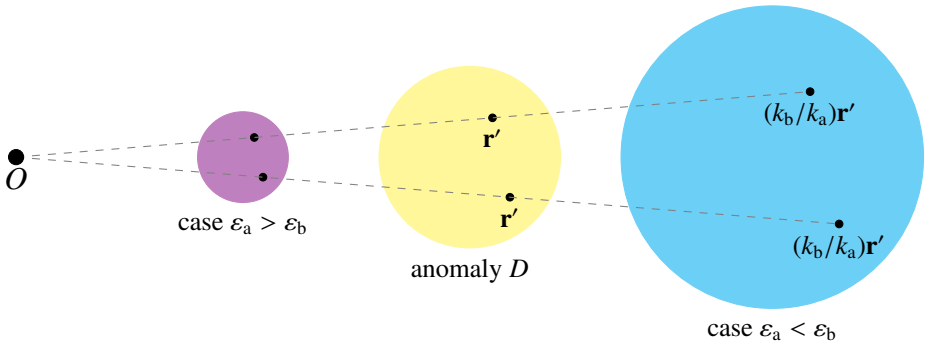

Figure 1. Description of the simulation result. Yellow-colored circle is the true anomaly and cyan- and violet-colored circles are retrieved anomalies through the map of $\mathfrak{F}(k_a, \mathbf{r})$.

Figure 2 shows maps of $\mathfrak{F}(k_a, \mathbf{r})$ with various selections of ε_a in the presence of D_1. As we discussed above, the location of the retrieved anomaly gets closer to the origin and it becomes smaller as the value of ε_a increases (here, $\varepsilon_a = 3\varepsilon_b, 10\varepsilon_b$). Otherwise, as the value of ε_a decreases (here, $\varepsilon_a = 0.5\varepsilon_b$), the identified location becomes far from the origin and the size becomes larger. If $\varepsilon_a = 0.01\varepsilon_b$ i.e., the value of ε_a is very small, it is difficult to distinguish the D_1 and artifacts.

Notice that since

$$J_s(|k_b\mathbf{r}' - k_a\mathbf{r}|) = J_s\left(|k_a|\left|\left(\frac{k_b}{k_a}\right)\mathbf{r}' - \mathbf{r}\right|\right) := J_s(|k_a||\mathbf{r}'' - \mathbf{r}|),$$

due to the oscillating property of the Bessel function, several artifacts will be included in the map of $\mathfrak{F}(k_a, \mathbf{r})$ if $|k_a|$ is large, i.e., the value of ε_a is large enough compared to ε_b. In contrast, the map of $\mathfrak{F}(k_a, \mathbf{r})$ will contain no artifacts but the imaging result will be blurred if the value of ε_a is small enough compared to ε_b. This is the reason why several artifacts are included in the map of $\mathfrak{F}(k_a, \mathbf{r})$ when $\varepsilon_a = 10\varepsilon_b$ and why the obtained image is blurred when $\varepsilon_a = 0.1\varepsilon_b$ and $\varepsilon_a = 0.01\varepsilon_b$. We can observe the same phenomenon in the presence of multiple anomalies D_1 and D_2, as shown in the Figure 3.

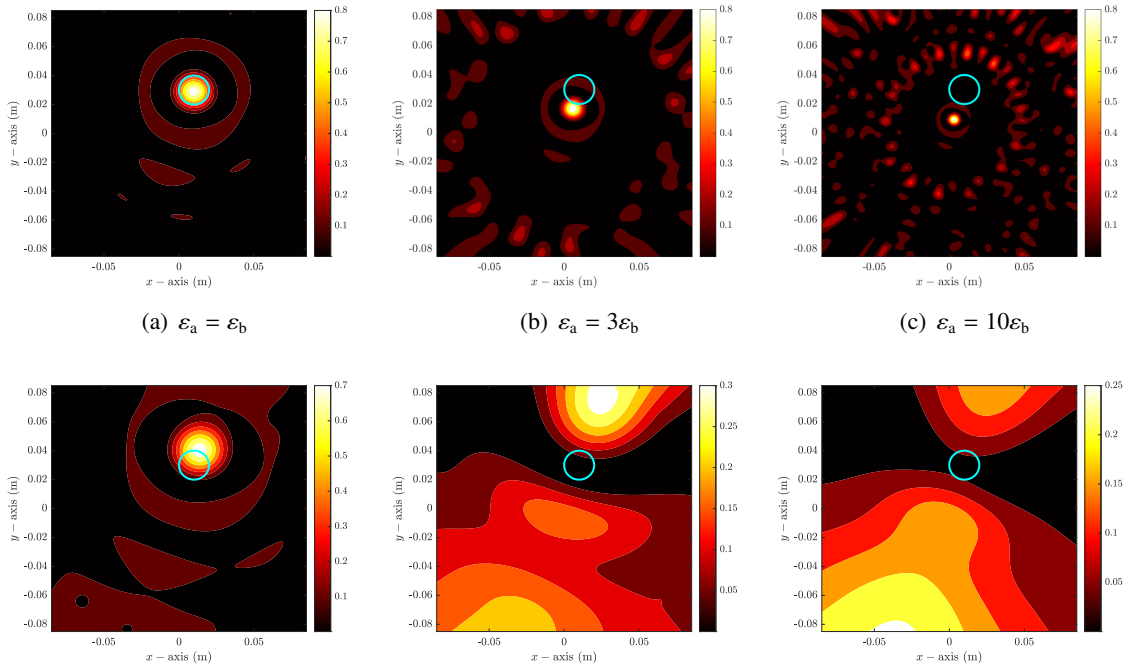

(a) $\varepsilon_a = \varepsilon_b$ (b) $\varepsilon_a = 3\varepsilon_b$ (c) $\varepsilon_a = 10\varepsilon_b$

(d) $\varepsilon_a = 0.5\varepsilon_b$ (e) $\varepsilon_a = 0.1\varepsilon_b$ (f) $\varepsilon_a = 0.01\varepsilon_b$

Figure 2. Maps of $\mathfrak{F}(k_a, \mathbf{r})$ at $f = 1.24$ GHz when $\sigma_a = \sigma_b$.

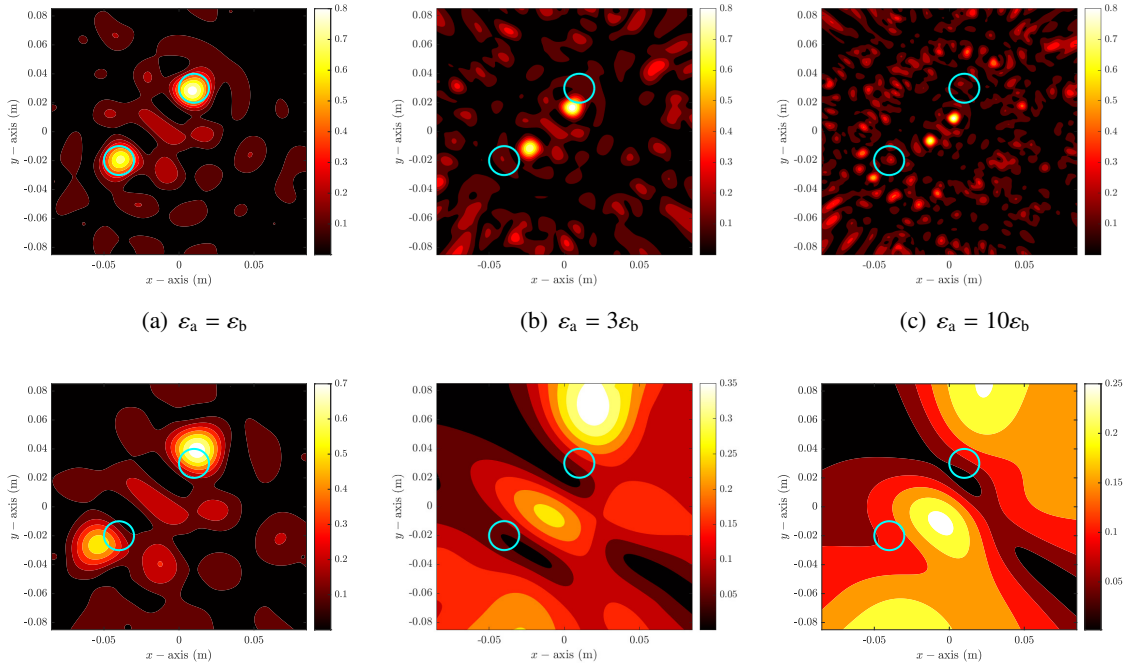

(a) $\varepsilon_a = \varepsilon_b$ (b) $\varepsilon_a = 3\varepsilon_b$ (c) $\varepsilon_a = 10\varepsilon_b$

(d) $\varepsilon_a = 0.5\varepsilon_b$ (e) $\varepsilon_a = 0.1\varepsilon_b$ (f) $\varepsilon_a = 0.01\varepsilon_b$

Figure 3. Maps of $\mathfrak{F}(k_a, \mathbf{r})$ at $f = 1.24$ GHz when $\varepsilon_a = \varepsilon_b$.

Example 4.2. *(Only exact value of σ_b is unknown) Next, we consider the case where only the exact value of σ_b is unknown and apply an alternative one σ_a such that*

$$k_a = \omega\sqrt{\mu_b\left(\varepsilon_b - i\frac{\sigma_a}{\omega}\right)}.$$

Same as the Example 4.1, if σ_a satisfies $\omega\varepsilon_a \gg \sigma_a$, the identified location becomes

$$\mathbf{r} = \left(\frac{k_b}{k_a}\right)\mathbf{r}' = \sqrt{\frac{\omega\varepsilon_b - i\sigma_b}{\omega\varepsilon_b - i\sigma_a}}\mathbf{r}' \approx \sqrt{\frac{\varepsilon_b}{\varepsilon_b}}\mathbf{r}' = \mathbf{r}' \quad \textit{for each} \quad \mathbf{r}' \in D_1. \tag{4.2}$$

Hence, it will be possible to retrieve almost accurate shapes and locations of anomalies when σ_a is sufficiently small.

Figure 4 shows maps of $\mathfrak{F}(k_a, \mathbf{r})$ with various selections of σ_a in the presence of D_1. In contrast to the results in Example 4.1, almost the exact location and shape of D_1 were retrieved if $\sigma_a < 3\sigma_b$, i.e., when σ_a was sufficiently small. The location of the retrieved anomaly gets closer to the origin and its size becomes smaller as the value of ε_a increases (here, $\varepsilon_a = 3\varepsilon_b, 10\varepsilon_b$). Unfortunately, it is very difficult to recognize D_1 due to the appearance of a huge artifact with a large magnitude if σ_a is not small $\sigma_a = 10\sigma_b = 2\,\mathrm{S/m}$.

We can observe the same phenomenon in the presence of multiple anomalies D_1 and D_2, as shown in the Figure 5, and conclude that it will be possible to retrieve the accurate shape and location of anomalies by choosing a very small (close to zero) value of σ_a when the exact value of background permittivity is known.

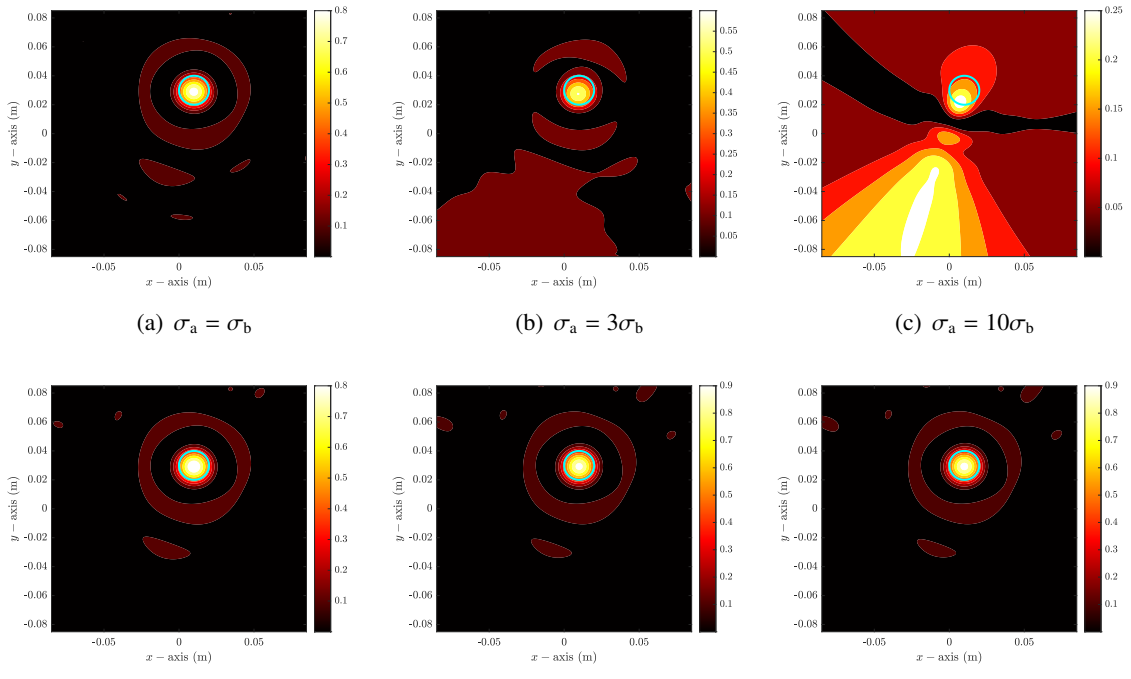

(a) $\sigma_a = \sigma_b$ (b) $\sigma_a = 3\sigma_b$ (c) $\sigma_a = 10\sigma_b$

(d) $\sigma_a = 0.5\sigma_b$ (e) $\sigma_a = 0.1\sigma_b$ (f) $\sigma_a = 0.01\sigma_b$

Figure 4. Maps of $\mathfrak{F}(k_a, \mathbf{r})$ at $f = 1.24\,\mathrm{GHz}$.

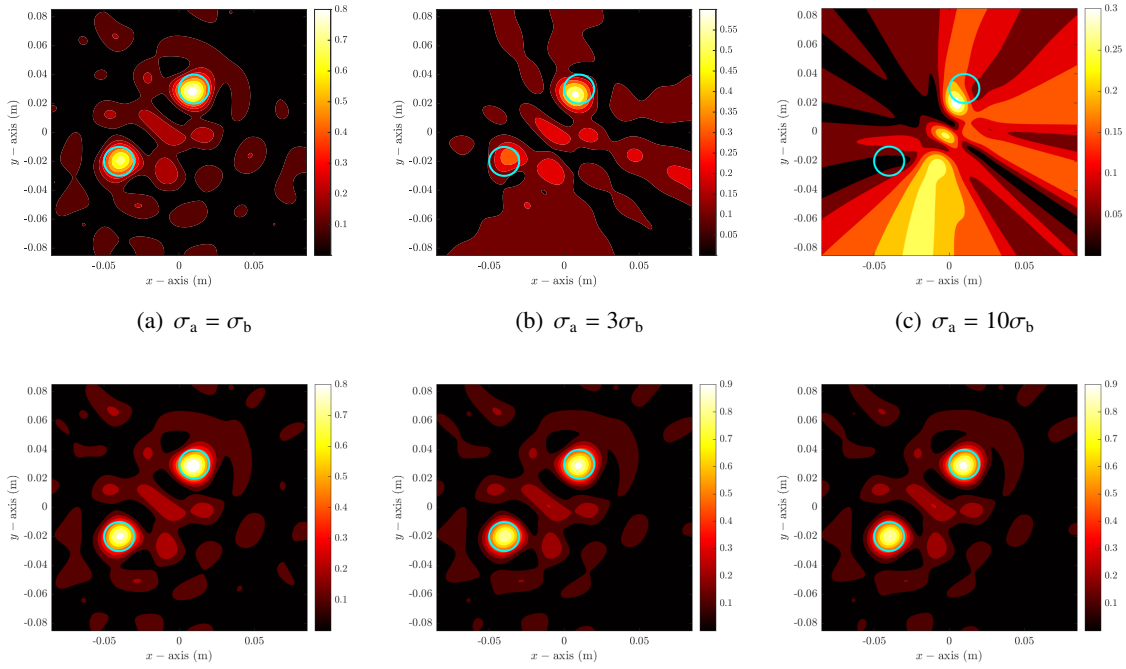

(a) $\sigma_a = \sigma_b$ (b) $\sigma_a = 3\sigma_b$ (c) $\sigma_a = 10\sigma_b$

(d) $\sigma_a = 0.5\sigma_b$ (e) $\sigma_a = 0.1\sigma_b$ (f) $\sigma_a = 0.01\sigma_b$

Figure 5. Maps of $\mathfrak{F}(k_a, \mathbf{r})$ at $f = 1.24\,\text{GHz}$.

Example 4.3. *(Identification of circle and rectangular shaped anomalies) Here, we consider the imaging of anomalies with different shapes. To this end, we applied* $f = 1.0\,\text{GHz}$, *used* $N = 36$ *antennas* $\mathbf{A}_n$, *and selected* D_1 *as a ball of Examples 4.1 and 4.3 except* $(\varepsilon_1, \sigma_1) = (45\varepsilon_0, 1.0\,\text{S/m})$, *and* D_2 *as a square with vertices* $(-0.05, -0.03)$, $(-0.03, -0.03)$, $(-0.03, -0.01)$ *and* $(-0.05, -0.01)$ *with* $(\varepsilon_2, \sigma_2) = (45\varepsilon_0, 1.0\,\text{S/m})$. *With this configuration, the scattering parameter data were generated by using the FEKO (Feldberechnung für Körper mit beliebiger Oberfläche).*

Figure 6 shows maps of $\mathfrak{F}(k_a, \mathbf{r})$ *when* $\varepsilon_a \neq \varepsilon_b$ *and* $\sigma_a = \sigma_b$. *Similar to the results in Example 4.1, identified anomalies are concentrated at the origin and their retrieved sizes are smaller than the true one when* $\varepsilon_a > \varepsilon_b$. *Moreover, identified anomalies located far from the origin and their retrieved sizes are larger than the true one when* $\varepsilon_a < \varepsilon_b$. *However, opposite to the results in Examples 4.1 and 4.3, it is hard to recognize the shape of* D_1 *and* D_2 *due to the appearance of several artifacts in the neighborhood of anomalies.*

Figure 7 shows maps of $\mathfrak{F}(k_a, \mathbf{r})$ *when* $\varepsilon_a = \varepsilon_b$ *and* $\sigma_a \neq \sigma_b$. *Similar to the results in Example 4.3, we can examine that it is possible to recognize the outline shape of anomalies by choosing a very small value of* σ_a. *However, exact shape of anomalies cannot be retrieved still.*

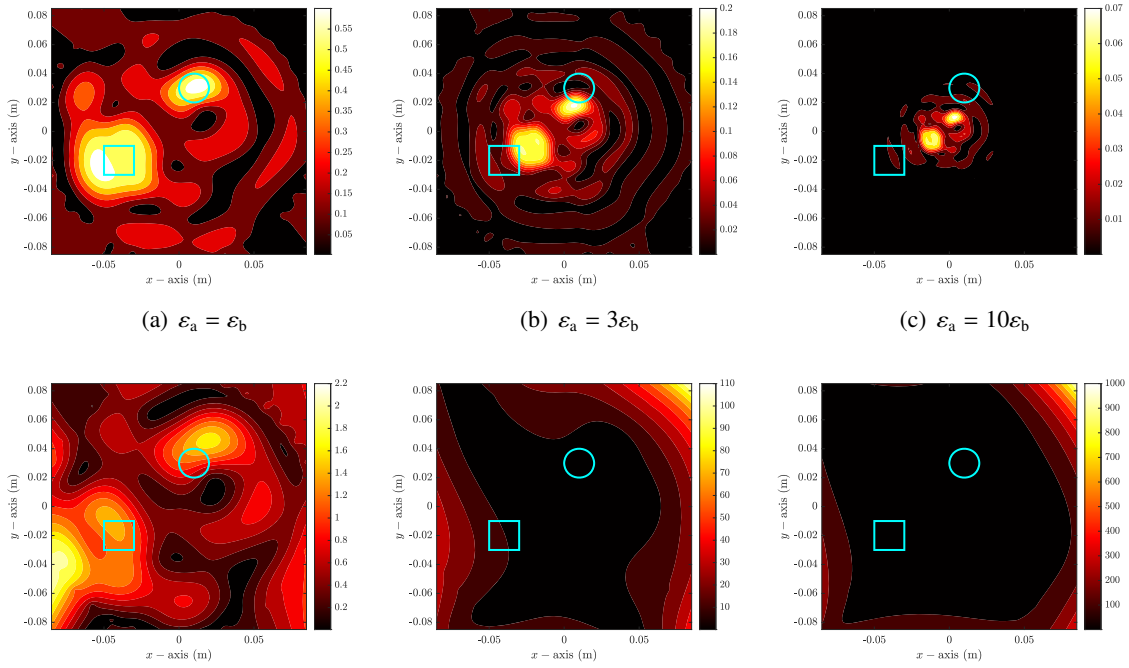

(a) $\varepsilon_a = \varepsilon_b$ (b) $\varepsilon_a = 3\varepsilon_b$ (c) $\varepsilon_a = 10\varepsilon_b$

(d) $\varepsilon_a = 0.5\varepsilon_b$ (e) $\varepsilon_a = 0.1\varepsilon_b$ (f) $\varepsilon_a = 0.01\varepsilon_b$

Figure 6. Maps of $\mathfrak{F}(k_a, \mathbf{r})$ at $f = 1$ GHz when $\sigma_a = \sigma_b$.

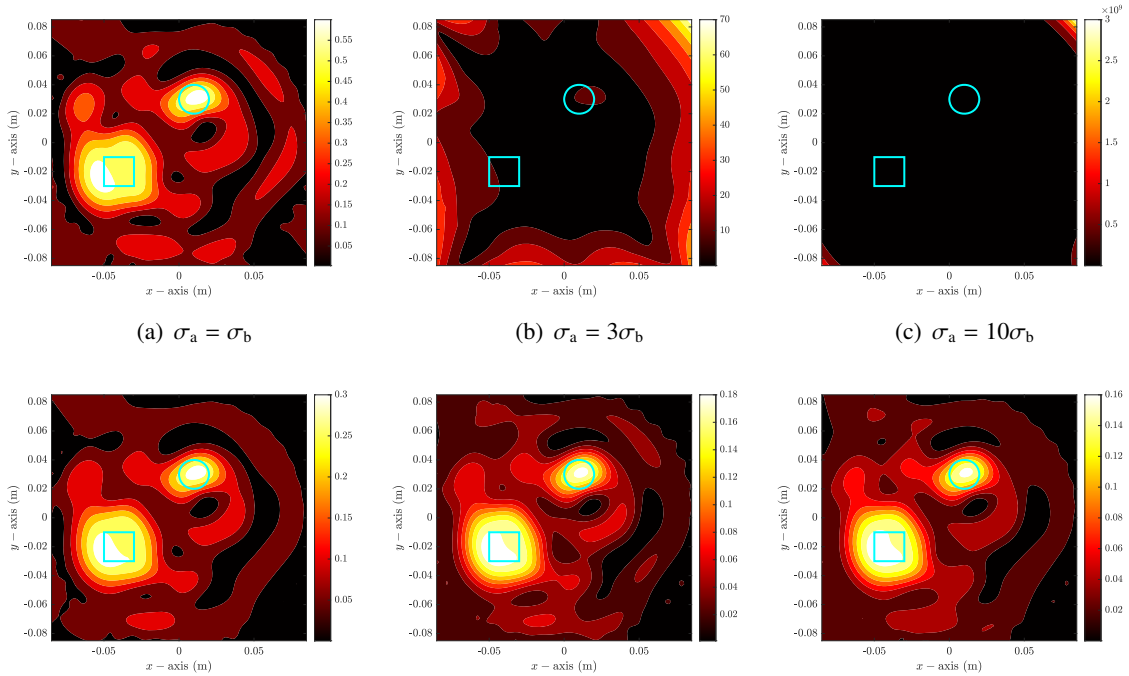

(a) $\sigma_a = \sigma_b$ (b) $\sigma_a = 3\sigma_b$ (c) $\sigma_a = 10\sigma_b$

(d) $\sigma_a = 0.5\sigma_b$ (e) $\sigma_a = 0.1\sigma_b$ (f) $\sigma_a = 0.01\sigma_b$

Figure 7. Maps of $\mathfrak{F}(k_a, \mathbf{r})$ at $f = 1$ GHz.

5. Conclusions

The structure of the imaging function of SM for retrieving small anomalies from scattering matrix is revealed when complete information of the background medium is not available. On the basis of its relationship with the infinite series of Bessel function of the first kind, we have theoretically confirmed why the accurate shape and location of anomalies cannot be retrieved.

The main subject of this paper is the imaging of small anomaly in two-dimensional microwave imaging. An extension to multiple, small anomalies will be carried out in forthcoming work. Moreover, the development of an effective algorithm for retrieving the exact value of background wavenumber will be an interesting research subject. Finally, we expect that the methodology presented in this paper could be applied to real-world microwave imaging with inhomogeneous background.

Use of AI tools declaration

The author declares he has not used Artificial Intelligence (AI) tools in the creation of this article.

Acknowledgments

The author would like to acknowledge anonymous reviewers for their comments that help to increase the quality of the paper. The author is also grateful to Sangwoo Kang, Kwang-Jae Lee and Seong-Ho Son for helping in generating scattering parameter data. This work was supported by the research program of the Kookmin University.

Conflict of interest

The author declares no conflicts of interest regarding the publication of this paper.

References

1. S. Ahmad, T. Strauss, S. Kupis, T. Khan, Comparison of statistical inversion with iteratively regularized Gauss Newton method for image reconstruction in electrical impedance tomography, *Appl. Math. Comput.*, **358** (2019), 436–448. https://doi.org/10.1016/j.amc.2019.03.063
2. M. N. Akinci, Improving near-field orthogonality sampling method for qualitative microwave imaging, *IEEE T. Antenna. Propag.*, **66** (2018), 5475–5484. https://doi.org/10.1109/TAP.2018.2860123
3. H. Ammari, P. Garapon, F. Jouve, H. Kang, M. Lim, S. Yu, A new optimal control approach for the reconstruction of extended inclusions, *SIAM J. Control Optim.*, **51** (2013), 1372–1394. https://doi.org/10.1137/100808952
4. H. Ammari, J. Garnier, H. Kang, W. K. Park, K. Sølna, Imaging schemes for perfectly conducting cracks, *SIAM J. Appl. Math.*, **71** (2011), 68–91. https://doi.org/10.1137/100800130
5. H. Ammari, E. Iakovleva, S. Moskow, Recovery of small inhomogeneities from the scattering amplitude at a fixed frequency, *SIAM J. Math. Anal.*, **34** (2003), 882–900. https://doi.org/10.1137/S0036141001392785

6. H. Ammari, S. Moskow, M. Vogelius, Boundary integral formulas for the reconstruction of electromagnetic imperfections of small diameter, *ESAIM Control Optim. Ca.*, **9** (2003), 49–66. https://doi.org/10.1051/cocv:2002071
7. H. Ammari, M. Vogelius, D. Volkov, Asymptotic formulas for perturbations in the electromagnetic fields due to the presence of imperfections of small diameter II. the full Maxwell equations, *J. Math. Pure. Appl.*, **80** (2001), 769–814. https://doi.org/10.1016/S0021-7824(01)01217-X
8. L. Audibert, H. Haddar, The generalized linear sampling method for limited aperture measurements, *SIAM J. Imaging Sci.*, **10** (2017), 845–870. https://doi.org/10.1137/16M110112X
9. L. Borcea, G. Papanicolaou, F. G. Vasquez, Edge illumination and imaging of extended reflectors, *SIAM J. Imaging Sci.*, **1** (2008), 75–114. https://doi.org/10.1137/07069290X
10. Y. Boukari, H. Haddar, The factorization method applied to cracks with impedance boundary conditions, *Inverse Probl. Imag.*, **7** (2013), 1123–1138. https://doi.org/10.3934/ipi.2013.7.1123
11. A. E. Bulyshev, S. Y. Semenov, A. E. Souvorov, R. H. Svenson, A. G. Nazarov, Y. E. Sizov, et al., Computational modeling of three-dimensional microwave tomography of breast cancer, *IEEE T. Bio-Med. Eng.*, **48** (2001), 1053–1056. https://doi.org/10.1109/10.942596
12. R. Chandra, H. Zhou, I. Balasingham, R. M. Narayanan, On the opportunities and challenges in microwave medical sensing and imaging, *IEEE T. Bio.-Med. Eng.*, **62** (2015), 1667–1682. https://doi.org/10.1109/TBME.2015.2432137
13. W. C. Chew, Y. M. Wang, Reconstruction of two-dimensional permittivity distribution using the distorted born iterative method, *IEEE T. Med. Imaging*, **9** (1990), 218–225. https://doi.org/10.1109/42.56334
14. D. Colton, R. Kress, *Inverse acoustic and electromagnetic scattering problems*, Mathematics and Applications Series, New York: Springer, 1998. https://doi.org/10.1007/978-1-4614-4942-3
15. H. Diao, X. Cao, H. Liu, On the geometric structures of transmission eigenfunctions with a conductive boundary condition and applications, *Commun. Part. Diff. Eq.*, **46** (2021), 630–679. https://doi.org/10.1080/03605302.2020.1857397
16. O. Dorn, D. Lesselier, Level set methods for inverse scattering, *Inverse Probl.*, **22** (2006), R67–R131. https://doi.org/10.1088/0266-5611/22/4/R01
17. A. Franchois, C. Pichot, Microwave imaging-complex permittivity reconstruction with a Levenberg-Marquardt method, *IEEE T. Antenn. Propag.*, **45** (1997), 203–215. https://doi.org/10.1109/8.560338
18. N. I. Grinberg, A. Kirsch, The factorization method for obstacles with a-priori separated sound-soft and sound-hard parts, *Math. Comput. Simulat.*, **66** (2004), 267–279. https://doi.org/10.1016/j.matcom.2004.02.011
19. M. Haynes, J. Stang, M. Moghaddam, Real-time microwave imaging of differential temperature for thermal therapy monitoring, *IEEE T. Bio.-Med. Eng.*, **61** (2014), 1787–1797. https://doi.org/10.1109/TBME.2014.2307072
20. D. Ireland, K. Bialkowski, A. Abbosh, Microwave imaging for brain stroke detection using Born iterative method, *IET Microw. Antenna. P.*, **7** (2013), 909–915. https://doi.org/10.1049/iet-map.2013.0054

21. N. Irishina, O. Dorn, M. Moscoso, A level set evolution strategy in microwave imaging for early breast cancer detection, *Comput. Math. Appl.*, **56** (2008), 607–618. https://doi.org/10.1016/j.camwa.2008.01.004

22. K. Ito, B. Jin, J. Zou, A direct sampling method to an inverse medium scattering problem, *Inverse Probl.*, **28** (2012), 025003. https://doi.org/10.1088/0266-5611/28/2/025003

23. S. Kang, M. Lambert, W. K. Park, Direct sampling method for imaging small dielectric inhomogeneities: Analysis and improvement, *Inverse Probl.*, **34** (2018), 095005. https://doi.org/10.1088/1361-6420/aacf1d

24. A. Kirsch, S. Ritter, A linear sampling method for inverse scattering from an open arc, *Inverse Probl.*, **16** (2000), 89–105. https://doi.org/10.1088/0266-5611/16/1/308

25. O. Kwon, J. K. Seo, J. R. Yoon, A real-time algorithm for the location search of discontinuous conductivities with one measurement, *Commun. Pur. Appl. Math.*, **55** (2002), 1–29. https://doi.org/10.1002/cpa.3009

26. Z. Liu, A new scheme based on Born iterative method for solving inverse scattering problems with noise disturbance, *IEEE Geosci. Remote S.*, **16** (2019), 1021–1025. https://doi.org/10.1109/LGRS.2019.2891660

27. F. L. Louër, M. L. Rapún, Topological sensitivity for solving inverse multiple scattering problems in 3D electromagnetism. Part I: One step method, *SIAM J. Imaging Sci.*, **10** (2017), 1291–1321. https://doi.org/10.1137/17M1113850

28. R. Palmeri, M. T. Bevacqua, L. Crocco, T. Isernia, L. D. Donato, Microwave imaging via distorted iterated virtual experiments, *IEEE T. Antenn. Propag.*, **65** (2017), 829–838. https://doi.org/10.1109/TAP.2016.2633070

29. W. K. Park, Multi-frequency subspace migration for imaging of perfectly conducting, arc-like cracks in full- and limited-view inverse scattering problems, *J. Comput. Phys.*, **283** (2015), 52–80. http://dx.doi.org/10.1016/j.jcp.2014.11.036

30. W. K. Park, A novel study on subspace migration for imaging of a sound-hard arc, *Comput. Math. Appl.*, **74** (2017), 3000–3007. http://dx.doi.org/10.1016/j.camwa.2017.07.045

31. W. K. Park, Performance analysis of multi-frequency topological derivative for reconstructing perfectly conducting cracks, *J. Comput. Phys.*, **335** (2017), 865–884.

32. W. K. Park, Real-time microwave imaging of unknown anomalies via scattering matrix, *Mech. Syst. Signal Pr.*, **118** (2019), 658–674. https://doi.org/10.1016/j.ymssp.2018.09.012

33. W. K. Park, Experimental validation of the factorization method to microwave imaging, *Results Phys.*, **17** (2020), 103071. https://doi.org/10.1016/j.rinp.2020.103071

34. W. K. Park, Application of MUSIC algorithm in real-world microwave imaging of unknown anomalies from scattering matrix, *Mech. Syst. Signal Pr.*, **153** (2021), 107501. https://doi.org/10.1016/j.ymssp.2020.107501

35. W. K. Park, A novel study on the MUSIC-type imaging of small electromagnetic inhomogeneities in the limited-aperture inverse scattering problem, *J. Comput. Phys.*, **460** (2022), 111191. https://doi.org/10.1016/j.jcp.2022.111191

36. W. K. Park, Real-time detection of small anomaly from limited-aperture measurements in real-world microwave imaging, *Mech. Syst. Signal Pr.*, **171** (2022), 108937. https://doi.org/10.1016/j.ymssp.2022.108937

37. W. K. Park, On the application of orthogonality sampling method for object detection in microwave imaging, *IEEE T. Antenn. Propag.*, **71** (2023), 934–946. https://doi.org/10.1109/TAP.2022.3220033

38. W. K. Park, H. P. Kim, K. J. Lee, S. H. Son, MUSIC algorithm for location searching of dielectric anomalies from S-parameters using microwave imaging, *J. Comput. Phys.*, **348** (2017), 259–270. http://dx.doi.org/10.1016/j.jcp.2017.07.035

39. W. K. Park, D. Lesselier, Reconstruction of thin electromagnetic inclusions by a level set method, *Inverse Probl.*, **25** (2009), 085010. https://doi.org/10.1088/0266-5611/25/8/085010

40. R. Potthast, A study on orthogonality sampling, *Inverse Probl.*, **26** (2010), 074015. https://doi.org/10.1088/0266-5611/26/7/074015

41. D. M. Pozar, *Microwave engineering*, 4 Eds., John Wiley & Sons, 2011.

42. M. Slaney, A. C. Kak, L. E. Larsen, Limitations of imaging with first-order diffraction tomography, *IEEE T. Microw. Theory*, **32** (1984), 860–874. https://doi.org/10.1109/TMTT.1984.1132783

43. S. H. Son, K. J. Lee, W. K. Park, Application and analysis of direct sampling method in real-world microwave imaging, *Appl. Math. Lett.*, **96** (2019), 47–53. https://doi.org/10.1016/j.aml.2019.04.016

44. S. H. Son, N. Simonov, H. J. Kim, J. M. Lee, S. I. Jeon, Preclinical prototype development of a microwave tomography system for breast cancer detection, *ETRI J.*, **32** (2010), 901–910. https://doi.org/10.4218/etrij.10.0109.0626

45. A. Timonov, M. V. Klibanov, A new iterative procedure for the numerical solution of coefficient inverse problems, *Appl. Numer. Math.*, **55** (2005), 191–203. https://doi.org/10.1016/j.apnum.2004.09.031

46. W. Yin, H. Qi, P. Meng, Broad learning system with preprocessing to recover the scattering obstacles with far-field data, *Adv. Appl. Math. Mech.*, **15** (2023), 984–1000. https://doi.org/10.4208/aamm.OA-2021-0352

47. Y. Yin, W. Yin, P. Meng, H. Liu, The interior inverse scattering problem for a two-layered cavity using the bayesian method, *Inverse Probl. Imag.*, **16** (2022), 673–690. https://doi.org/10.3934/ipi.2021069

48. D. Zhang, Y. Guo, Y. Wang, Y. Chang, Co-inversion of a scattering cavity and its internal sources: Uniqueness, decoupling and imaging, *Inverse Probl.*, **39** (2023), 065004. https://doi.org/10.1088/1361-6420/accc4f

AIMS Press